Real-Time Interfacial Nanothermometry Using DNA-PAINT Microscopy

Document Version:
Publisher's PDF, also known as Version of Record (includes final page, issue and volume numbers)

Please check the document version of this publication:

• A submitted manuscript is the version of the article upon submission and before peer-review. There can be important differences between the submitted version and the official published version of record. People interested in the research are advised to contact the author for the final version of the publication, or visit the DOI to the publisher's website.
• The final author version and the galley proof are versions of the publication after peer review.
• The final published version features the final layout of the paper including the volume, issue and page numbers.

Link to publication

Real-Time Interfacial Nanothermometry Using DNA-PAINT Microscopy

Sjoerd W. Nooteboom, Yuyang Wang, Swayandipta Dey, and Peter Zijlstra*

Biofunctionalized nanoparticles are increasingly used in biomedical applications including sensing, targeted delivery, and hyperthermia. However, laser excitation and associated heating of the nanomaterials may alter the structure and interactions of the conjugated biomolecules. Currently no method exists that directly monitors the local temperature near the material's interface where the conjugated biomolecules are. Here, a nanothermometer is reported based on DNA-mediated points accumulation for imaging nanoscale topography (DNA-PAINT) microscopy. The temperature dependent kinetics of repeated and reversible DNA interactions provide a direct readout of the local interfacial temperature. The accuracy and precision of the method is demonstrated by measuring the interfacial temperature of many individual gold nanoparticles in parallel, with a precision of 1 K. In agreement with numerical models, large particle-to-particle differences in the interfacial temperature are found due to underlying differences in optical and thermal properties. In addition, the reversible DNA interactions enable the tracking of interfacial temperature in real-time with intervals of a few minutes. This method does not require prior knowledge of the optical and thermal properties of the sample, and therefore opens the window to understanding and controlling interfacial heating in a wide range of nanomaterials.

1. Introduction

Nanoparticles (NPs) have emerged as a revolutionary material with unique optical, mechanical, and thermal properties that are governed by their large surface-to-volume ratio. As a result, NPs are used in a range of applications, notably in the biomedical field where they are used as biosensors,[1] drug delivery vehicles,[2] and agents for photothermal therapy.[3–7] In particular, metallic NPs exhibit plasmon resonances that result in

strong absorption and scattering of light by the particles that has been exploited for the detection and spectroscopy of individual NPs.[8,9] As a direct result, plasmonic nanoparticles have also been used as a sensitive and specific optical platform for a range of single-particle and single-molecule sensors that exploit plasmon-enhanced fluorescence[10–15] or label-free mechanisms.[16–18]

These applications mostly use optical excitation of the NPs which, due to the thermoplasmonic effect caused by photon absorption, induces a strong temperature gradient around the NPs.[19] Such local heating has been exploited for bioassays,[18,20–22] hyperthermia therapy,[3–7] photothermal chemistry,[23,24] and photovoltaics.[25,26] In the light of biomedical applications, though, heating is an effect that must be carefully controlled because it can alter biomolecular interaction dynamics and eventually cause denaturation of the conjugated biomolecules.[19] The application of NPs for biomolecular studies therefore requires quantitative understanding of the interplay between optical excitation and the temperature near the interface of the NP (where the biomolecules are conjugated).

As a result several methods have appeared that probe the temperature of single NPs,[27] which can roughly be divided into three categories. The first includes methods that probe the temperature of the metal (inside the NP), most prominently anti-Stokes Raman scattering.[28–31] Second, methods based on photothermal microscopy[18,20] or interferometry[32–34] probe local refractive index changes induced by heat conduction across several microns into the surrounding medium. In both approaches the interfacial temperature can be extracted using thermodynamic models,[32,33] but these require knowledge of the size and shape of each individual particle and its interfacial thermal resistance. These properties vary from particle-to-particle and cannot be extracted easily or remain unknown altogether.[29] Third, solution-phase probes such as dyes or quantum dots have been employed[35] that change fluorescence spectrum,[36] intensity,[37,38] or polarization anisotropy[39] as a function of temperature. Interfacial temperatures can however not be extracted because the signals are averaged over the whole diffraction limited focal spot and can be modified by the particle.

Recently, thermometry methods based on nucleic acids have been proposed that exploit temperature dependent

S. W. Nooteboom, Y. Wang, S. Dey, P. Zijlstra
Eindhoven University of Technology
Department of Applied Physics and Institute for Complex Molecular Systems
Eindhoven 5600 MB, The Netherlands
E-mail: p.zijlstra@tue.nl

ADVANCED
SCIENCE NEWS
www.advancedsciencenews.com

NANO · MICRO
small
www.small-journal.com

melting of DNA duplexes that are conjugated to the NP. The surface temperature is then quantified, for example by measuring the concentration of released DNA in solution,[40–42] or by quantifying the remaining single-stranded DNA on the surface of the sample.[43] Because these approaches require several sample preparation steps and use high-affinity DNA duplexes they only report the maximum temperature during the history of the sample, prohibiting real-time and spatially resolved thermometry.

Here we report a nanothermometer that uses low-affinity DNA interactions to continuously monitor the temperature near the interface of single nanoparticles. Using an approach based on DNA-mediated points accumulation for imaging nanoscale topography (DNA-PAINT) the kinetics of single-molecule DNA interactions are monitored in a wide-field microscope, providing a direct readout of the local interfacial temperature via the well-known temperature dependence of the average bound-state lifetime. We quantify the precision of the thermometer and compare the measured surface temperatures for both bulk and laser heating to numerical models. We show that this method enables continuous monitoring of the surface temperature at intervals of a few minutes with a precision of 1 K. Using this method we study the interplay between NP heating and plasmon-enhanced fluorescence intensity. This method of thermometry requires no prior knowledge of the thermal and optical properties of the sample and only requires one calibration for a given imaging buffer. It is therefore suitable to continuously monitor the surface temperature of a wide range of nanoscale structures that are used for example for biomedical, catalytic, and photovoltaic applications.

2. Results and Discussion

The approach toward interfacial thermometry that we adopted is based on DNA-PAINT,[15,44] and is detailed in **Figure 1**. The experiments were performed on an inverted total internal reflection fluorescence (TIRF) microscope equipped with a flow chamber that contained immobilized gold nanorods (AuNRs), with an average size of 92×40 nm^2 (see Figure S1, Supporting Information, for characterizations of the AuNRs). AuNRs were immobilized on a glass coverslip by spincoating, resulting in a sparse distribution of AuNRs on the surface that enabled single-particle studies. After extensive rinsing to remove residual surfactant, the AuNRs were functionalized with single-stranded DNA docking strands by incubation in a solution of thiolated DNA (see Experimental Section for a detailed sample preparation protocol). After removal of unconjugated docking strands the flow chamber was filled with a 9 nt complementary strand (imager) carrying ATTO655. The short complementary region results in repetitive and short-lived interactions with rate constants k_{on} and k_{off} (see Figure 1b).

On the camera, we observe the 1-photon luminescence (1-PL) of individual AuNRs as diffraction-limited spots (see Figure 1c). The intensity of AuNR luminescence varies, depending on plasmon wavelength, the local excitation power density, and orientation of the AuNR relative to the polarized laser excitation. The local laser power density near the glass–water interface was calculated based on the Gaussian profile of the beam and

the incident angle in the TIRF microscope (see Experimental Section for details).

DNA hybridization kinetics were monitored by capturing a time lapse and tracking the intensity of each AuNR over time, where we observe a stable baseline intensity due to 1-PL of the nanoparticle, upon which fluorescent bursts due to single imager binding events are superimposed (see Figure 1d). While bound to the AuNR the fluorescence of the imager is strongly enhanced compared to freely diffusing imagers due to plasmon-enhanced fluorescence. The high signal-to-noise ratio afforded by plasmon-enhanced fluorescence provides a reliable readout of the hybridization kinetics. The peak photon count rate (PCR) per event varies due to the different enhancement factors at different binding locations of the imagers, but our approach is insensitive to differences in plasmon-enhanced fluorescence intensity because the thermometer uses only the bound-state lifetime to estimate the interfacial temperature.

We now turn our attention to the analysis of the bound-state lifetime (t_{on}) of DNA-PAINT interactions and its temperature dependence. Imager binding events were identified by applying a threshold to the intensity timetraces of single AuNRs. The t_{on} value for each event was determined as the number of consecutive camera frames with an intensity above the threshold, multiplied by the camera frame interval (see the Supporting Information for details on the data analysis). Based on thermodynamic principles, it is expected that t_{on} values for different events within a timetrace are exponentially distributed with a mean value τ_{on} that decreases with temperature.[44] We initially studied this by varying the bulk solution temperature in the flow cell using a temperature-controlled sample stage (see Experimental Section). We varied the temperature of the stage between 292–307 K while keeping the laser power density at a minimum ($<10^7$ W m^{-2}) to minimize photothermal heating to $\ll 1$ K. In **Figure 2**a,b we show two timetraces recorded on the same AuNR but at different bulk temperatures, displaying a dramatic change in the bound-state lifetime of the events.

Figure 2c shows the cumulative distribution function (CDF) of t_{on}, representing the fraction of events with duration equal to or shorter than a given t_{on}, aggregated over all AuNRs in the field of view (FOV) at various bulk temperatures. At each temperature, we observe a clear exponential distribution as expected from a random process. The CDFs were fitted to a function of the form $CDF = 1 - A\exp\left(-\dfrac{t}{\tau_{on}}\right)$, where A and τ_{on} are fit parameters representing a normalization factor and the mean bound-state lifetime, respectively. The ensemble average value of τ_{on} decreases from 1.21 ± 0.03 s at 292 K to 0.11 ± 0.01 s at 305 K. We fitted the temperature-dependent bound-state lifetimes with the Arrhenius equation $\ln(k_{off}) = \dfrac{-E_a}{RT} + \ln A$, where $k_{off} = \dfrac{1}{\tau_{on}}$ is the dissociation rate constant, E_a is the activation energy of the dissociation reaction, R is the gas constant (8.314 J K^{-1} mol^{-1}), T is the temperature, and A is the pre-exponential factor of the reaction rate.[45,46] In the inset to Figure 2c we show the Arrhenius plot, which is linear as expected with $E_a = 36.5$ kcal mol^{-1} and $\ln A = 62.6$. These Arrhenius parameters provide a calibration that enables us to deduce the interfacial temperature of individual AuNRs, regardless of the heat source, from the measured τ_{on}. Note here that we found E_a and $\ln A$ about

ADVANCED
SCIENCE NEWS
www.advancedsciencenews.com

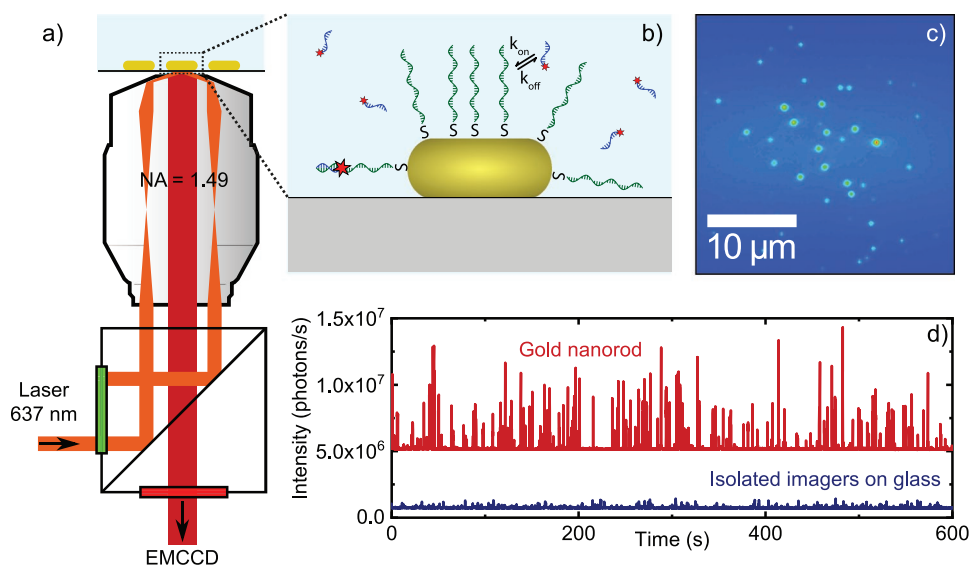NANO · MICRO
small
www.small-journal.com

Figure 1. Illustration of the experimental approach. a) Schematic of the TIRF microscopy setup. b) Schematic close-up of a single AuNR. DNA strands with conjugated dyes bind transiently to the docking strands on the AuNR surface. c) The laser illuminated region with many AuNRs as detected on the EMCCD camera. d) Example timetrace of a single AuNR as compared to nonspecific interactions on the glass. Traces have been offset vertically for clarity.

fourfold higher than those obtained for the same sequence by Jungmann et al.,[44] which we attribute to a different DNA-PAINT construct where docking strands were placed on DNA origamis instead of AuNRs.

Not every AuNR follows the exact same Arrhenius curve, as shown in the inset to Figure 2c and in Figure S2, Supporting Information. We hypothesize that differences in docking strand density on the AuNR surface influence the energy landscape of DNA interactions, and hence lead to slightly varying average bound-state lifetimes among AuNRs. This, along with stochastic variations in bound-state lifetime, introduces uncertainty in the temperature measurement from τ_{on}. To gauge this uncertainty, we show in Figure 2d the mean and standard deviation of determined temperatures of single AuNRs at each temperature setting. The mean closely follows the $y = x$ line, while the uncertainty in the temperature determination is 0.7 K (standard deviation). This represents the uncertainty in the measured temperature when using the ensemble-averaged Arrhenius fit in the inset of Figure 2c. In the further experiments on laser-induced heating, we combine this value with the statistical counting imprecision $1/\sqrt{N}$ in the determination of τ_{on}, where N is the number of detected events[47] (see the Supporting Information for details). The resulting overall uncertainty is then ≈1 K for AuNRs with ≈50 events. We note that, if each particle's response is individually calibrated before a measurement, the statistical precision dominates and the uncertainty is well below 1 K, but at the expense of experimental complexity because individual calibrations are needed before each measurement.

We used the aforementioned calibration results to measure the interfacial temperature induced by laser illumination at a constant ambient temperature of 295 K. A first illustration is given in **Figure 3**a,b, which shows two timetraces recorded on the same AuNR but at different excitation powers. At higher power, we naturally observe an increase in fluorescence

intensity, while the frequency of events is unchanged (k_{on} is not measurably affected). However, there is a clear decrease in the bound-state lifetime from 0.55 to 0.085 s due to the increased interfacial temperature. Using the calibration in Figure 2 we convert this decreased bound-state lifetime to a change in interfacial temperature from 296.1 to 305.3 K. Note that photobleaching plays a negligible role here because the short duration of the events is well below the characteristic time to bleaching for the stable ATTO dye that we employed.

The single-particle resolution of our approach enables us to map the temperature across the FOV, which is shown in Figure 3c. The size of the symbols in the spatial map depicts the mean dissociation rate k_{off} for each AuNR, reconstructed from different FOVs that were spatially overlapped. It is immediately apparent that the dissociation rate in the center of the Gaussian excitation beam is considerably higher than near the edges, providing a means to probe spatially dependent interfacial heating processes. Note that not all AuNRs in the center of the FOV exhibit a high interfacial temperature, likely caused by particle-to-particle variability in plasmon resonance and orientation that results in a different amount of absorbed laser energy.

In addition to interfacial temperature, the color coding in Figure 3c represents the PCR of the single-molecule plasmon-enhanced fluorescence. Two mechanisms contribute to a strong enhancement of the fluorescence signal compared to a freely diffusing dye: on the one hand the longitudinal plasmon resonance induces a strongly localized electric field around the AuNR that enhances the dye's excitation rate. On the other hand the dye's transition back to the ground state couples to the plasmon, increasing its decay rates and modifying the quantum yield of the emission. The total enhancement of the fluorescence intensity therefore depends strongly on the dye's intrinsic quantum yield,[48] but values in excess of 5000 have been achieved for low quantum yield dyes.[49] Here we used a fluorophore with an intrinsic quantum yield of 30% that binds
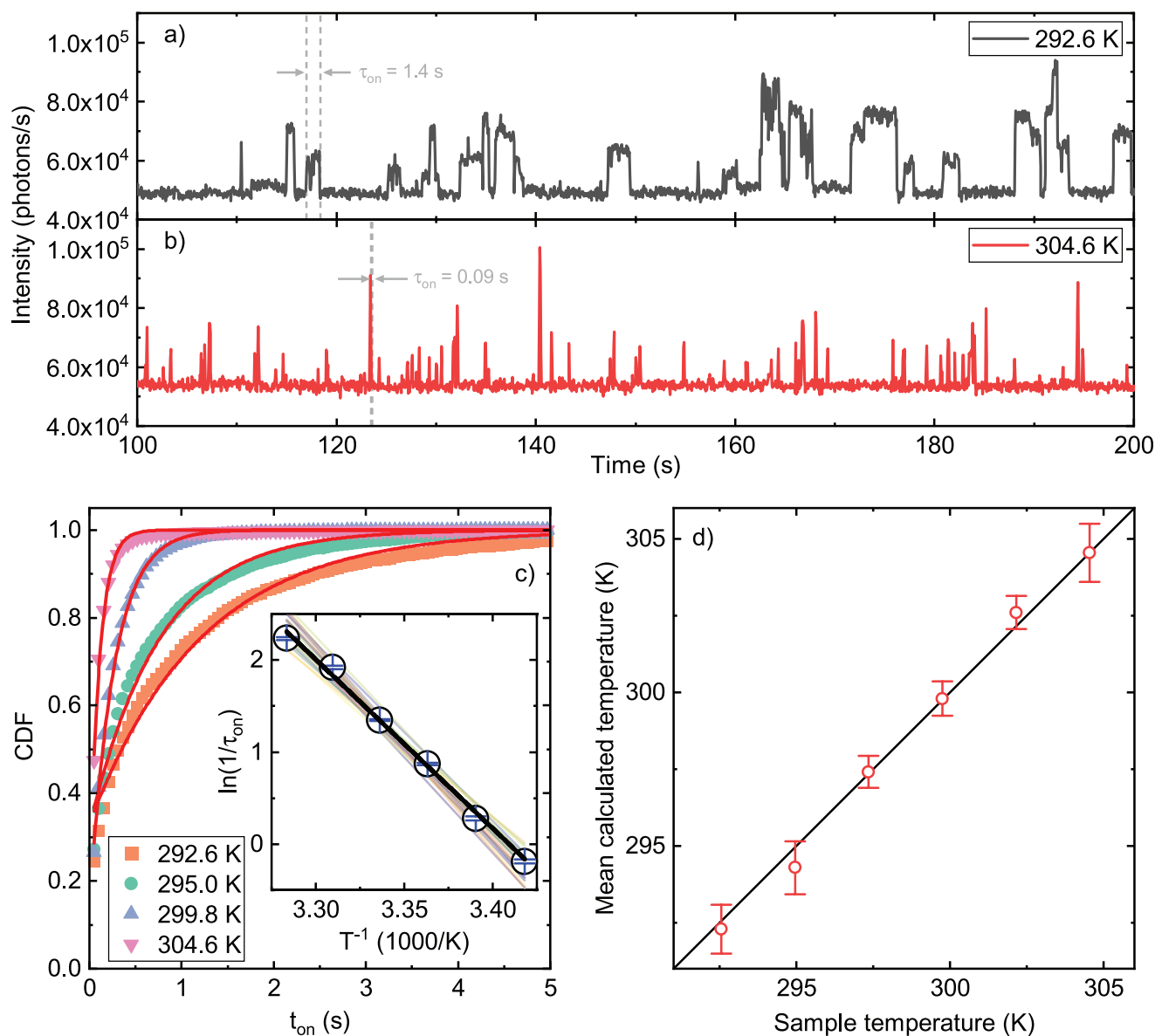
**ADVANCED
SCIENCE NEWS**

www.advancedsciencenews.com

NANO · MICRO

small

www.small-journal.com

Figure 2. Calibration of the temperature sensor. a,b) Zoom of timetraces of the same AuNR at 292.6 and 304.6 K. The mean bound-state lifetime for each timetrace is indicated on representative events. c) Cumulative distribution functions (CDF, markers) of the bound-state lifetime on all AuNRs in the FOV, and fits (red lines, see text for details). Inset: Mean bound-state lifetime τ_{on} averaged over all AuNRs as a function of temperature (black circles; blue error bars represent fit uncertainty). The data are plotted in Arrhenius form with a linear fit (black line); colored lines represent Arrhenius fits for individual AuNRs. d) Mean and standard deviation of the temperature of single AuNRs determined using the calibration in (c). The black line represents $y = x$.

≈2.5 nm from the AuNR surface,[15] yielding a fluorescence enhancement up to ≈20-fold (see Figures S3 and S4, Supporting Information).

The measured PCR is determined by averaging the photon emission rate over the ten brightest events in a 10 min time-trace.[15] Again, AuNRs in the center yield higher PCRs as they are more strongly excited. In fact, there is a clear correlation between PCR and temperature. This is shown in Figure 3d, which represents the same data as Figure 3c where k_{off} has been converted to temperature. The correlation can be fitted with a linear function, $T = b \times PCR + T_0$. The fit matches the data very well where we find $T_0 = 295.1$ K, essentially equal

to the lab temperature of 295 K. Hence, the burst intensity is indeed proportional to the degree of plasmonic heating, which is expected if both are mostly determined by the excitation strength of the plasmon.

The proportionality factor b from the linear fit is 1.17×10^{-6}. This implies that for average particles in our system, plasmon-enhanced dyes generate 8.5×10^5 photons s^{-1} for every K temperature rise on the AuNR surface. For a limited interfacial temperature rise of 10 K, plasmon-enhanced fluorescence therefore provides up to 10^7 photons s^{-1} which will provide exciting possibilities in the study of molecular dynamics on short timescales that are now not accessible due to the limited
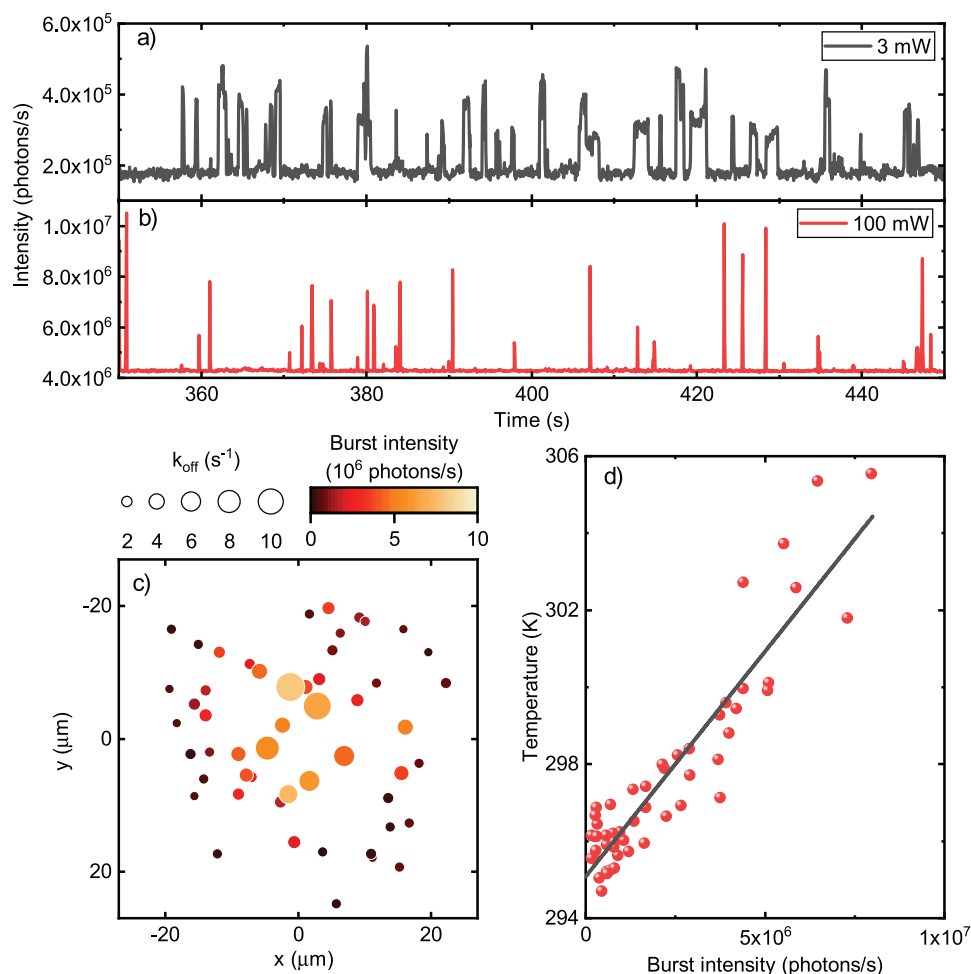
Figure 3. Effect of laser power density on DNA-mediated fluorescence bursts. a,b) Zoom of timetraces of the same AuNR at 3 and 100 mW laser power, revealing differences in bound-state lifetime and fluorescence intensity (note the different vertical axes). The frequency of events is 0.24 and 0.20 s^{-1}, respectively. c) The fitted k_{off} for each individual AuNR at 40 mW (overlay of three different FOVs), with colors indicating the burst intensity (average of the ten brightest events) of each AuNR. d) The burst intensity of each AuNR plotted against the surface temperature. Error bars omitted for clarity. The black line represents the linear fit $T = 1.17 \times 10^{-6}$PCR + 295.1.

brightness of a non-enhanced fluorophore. We consider this photons s^{-1} K^{-1} ratio a useful metric to gauge the performance of a plasmon-enhanced fluorescence sensor in situations where photothermal heating is an undesired side effect. The single-particle values of this metric vary between $0.1 - 3.0 \times 10^6$ photons s^{-1} K^{-1}, in good agreement with numerical simulations that indicate a range of $0.1 - 2.4 \times 10^6$ photons s^{-1} K^{-1} (vide infra for details on the heating simulations). Note that, even though the interfacial temperature and the PCR depend on the orientation of the AuNR in the partially polarized excitation field, the ratio of PCR to temperature loses this dependence (both scale linearly in absorbed laser power).

To further understand the photothermal heating we evaluated the temperature elevation on a nanorod surface induced by laser illumination using numerical simulations (see **Figure 4**a and Experimental Section; more details can be found in Figure S5, Supporting Information). We simulated an AuNR of 80×40 nm^2 that is illuminated on-resonance and oriented along the laser polarization in the center of the Gaussian beam. A numerical simulation of the absorption cross section of the

AuNR allowed us to calculate the amount of absorbed laser energy, which was used as a continuous source of internal heating. The simulated temperature increase of the AuNR interior is nearly 20 K at 2×10^8 W m^{-2}, close to the maximum power density in our setup. The temperature rapidly decays away from the AuNR surface in an approximately $1/r$ fashion, so the calculated temperature increase at 2.5 nm from the surface (the approximate position of the dye conjugated to the imager strand) is about 17.5 K. This constitutes the maximum expected temperature because in reality most AuNRs will have a different LSPR (hence a lower absorption cross section at 637 nm), a different orientation, and/or experience a lower power density. Therefore, given the lab temperature of about 295 K, we expect the surface temperature of all AuNRs to be below 315 K in our experiments at the highest laser power.

Next we evaluated the interfacial temperature of many AuNRs as a function of excitation power density. The experiment depicted by Figure 3c,d was repeated at a range of laser powers, and at each power we determined the local power density taking into account the Gaussian profile of the excitation
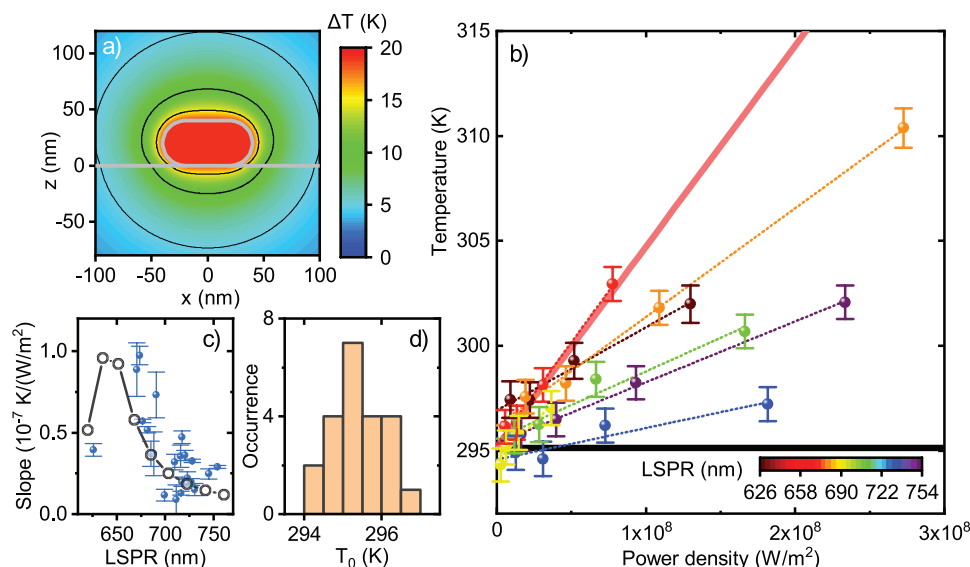
Figure 4. Power dependent interfacial temperature. a) Calculated temperature profile around a 80 × 40 nm² AuNR in water on a glass substrate at an illumination power density of 2 × 10⁸ W m⁻². Gray lines indicate the AuNR surface and the water–glass interface. b) Temperatures determined from τ_{on} for several AuNRs as a function of power density (laser power corrected for AuNR position), with colors indicating the LSPR. Dotted lines, linear fits; red line, calculated heating of the AuNR in (a); black line, lab temperature. c) Slope of the linear fits versus LSPR: blue points, experimental; black trace, simulation (AuNR interior). d) Histogram of T_0 values (intercept of the linear fits) for the full set of AuNRs.

beam and the total internal reflection excitation (see Experimental Section). The surface temperature of each individual AuNR was determined based on the fitted τ_{on} and the calibration curve. A plot of the particles' interfacial temperature revealed a linear dependence on power density, as expected (see Figure 4b and Figure S6, Supporting Information, for more data). In addition we observe a correlation of the particle temperature with the LSPR, as indicated by the line color in Figure 4b. Particles with an LSPR closer to the laser wavelength of 637 nm reach higher temperatures, as expected.

We compare the slope of the power dependence to numerical simulations in Figure 4c. The slope of the power dependent heating was simulated by calculating the absorption cross section for AuNRs with varying LSPR wavelengths, and converting this to an interfacial temperature. The measured slope varies strongly from particle to particle but a clear correlation is observed with the LSPR of the AuNRs. Compared to the simulated heating rate for AuNRs with varying LSPR wavelengths, the experimental data closely follow a trend wherein AuNRs that are excited close to their plasmon resonance experience more photothermal heating. Our method also reveals a strong heterogeneity (particle-to-particle differences) well beyond the precision of our measurement, even for AuNRs with the same plasmon wavelength. These particle-to-particle differences in heating likely originate from differences in volume, tip-shape, and local environment that affect the absorption cross section and the rate of heat dissipation into the substrate and medium. Although these parameters are difficult to take into account in the model (they depend on the atomic and molecular arrangement of the AuNR and its coating), knowledge of these parameters is not needed using our direct probe for local temperature.

The intercepts of the linear fits in Figure 4b represent the surface temperature at zero laser power T_0. We find a

distribution of values with $T_0 = 295.4 \pm 0.7$ K (see Figure 4d). This is very close to the lab temperature of 295 K, which again confirms the accuracy of the sensor. In addition, the precision of the T_0 determination is comparable to that found in the calibration above, confirming the robustness of the sensor.

The reversibility of the DNA interactions enables a continuous readout of single-nanoparticle temperature as shown in **Figure 5**. Here we quantified the temperature of single AuNRs that were exposed to an alternating sequence of excitation powers between 5 and 100 mW. The temperature was determined by splitting the timetraces into 3–5 min sections from which τ_{on} was extracted. With event frequencies typically between 0.1–0.5 s⁻¹ the value of τ_{on} was determined by an exponential fit to a few tens of events, giving a statistical τ_{on} precision of 10–20% and an absolute temperature precision of ≈1 K in our range of temperatures.

Figure 5a shows dark-field spectra of two AuNRs with different aspect ratios that result in different spectral overlap of the LSPR with the laser excitation wavelength. Both particles were positioned at the same distance from the center of the excitation beam to ensure a negligible difference in local laser power density (≈1.5 × 10⁸ W m⁻² at maximum laser power). Figure 5b,c shows the interfacial temperature change on the two AuNRs, monitored in real-time (see Figure S7, Supporting Information, for more data). The surface temperature of the shorter aspect ratio AuNR (blue spectrum in Figure 5a) clearly follows the alternations in power, and increases by ≈7.5 ± 1 K at the highest laser power density. The longer aspect ratio AuNR does not exhibit a significant temperature change at all due to the low absorption cross section at the laser wavelength. At the lowest laser power density the two AuNRs exhibit a slightly different temperature, which we attribute again to particle-to-particle variations in τ_{on} that are taken into account in the error bars as discussed above.

**ADVANCED
SCIENCE NEWS**

www.advancedsciencenews.com
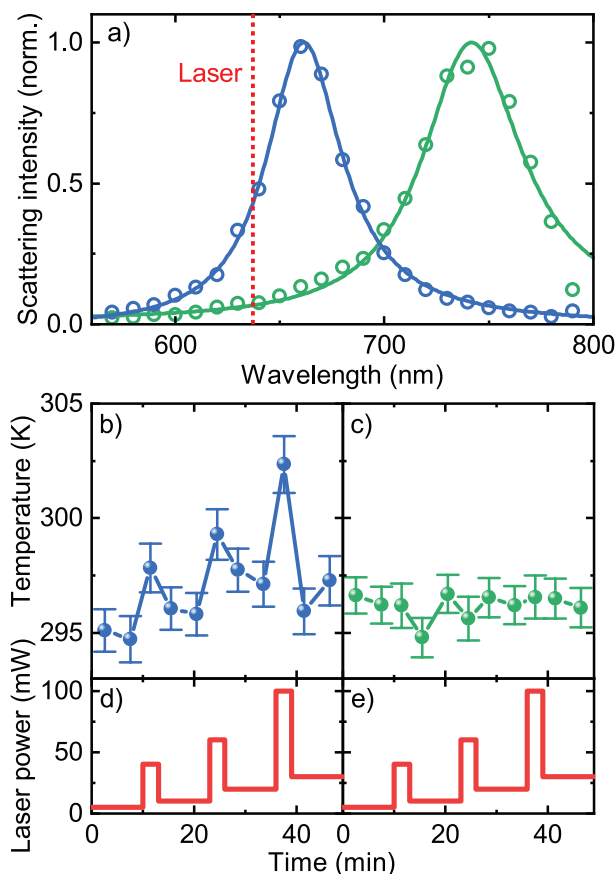
NANO · MICRO

small

www.small-journal.com

Figure 5. Real-time nanothermometry of interfacial temperature. a) Dark-field scattering spectra of two different AuNRs, one close to resonance with the laser and the other far from it. b,c) Interfacial temperatures determined at different points in time for the same two AuNRs. d,e) The laser power during the experiment depicted in panels (b,c).

The DNA-PAINT approach we presented quantifies the interfacial temperature of single nanoparticles with a precision of 1 K, which is very comparable to the precision of existing nanothermometry methods that measure the temperature of the solvent or the metal.[27] The accessible temperature range of our method is determined by the ability to quantify τ_{on} with the employed camera integration time of 50 ms. This allowed for the accurate determination of τ_{on} down to ≈100 ms, corresponding to a temperature rise of ≈10 K. Although methods such as Raman scattering have a larger dynamic range of several hundred Kelvin, such a dynamic range is not required in the context of biomedical applications where the maximum temperature rise should be limited to <10 K to prevent modification of the dynamics and structure of biomolecules. Furthermore, we note that the temperature range of the DNA-PAINT based method can be easily expanded by tuning the number of complementary nucleotides in the imager sequence.[40,42,43] This modifies the melting temperature of the DNA duplex and as a rough estimate, each added base pair increases τ_{on} by a factor of 2–4,[50] shifting the accessible temperature range by ≈5–10 K. This would enable the application of interfacial thermometry to the higher temperatures that are relevant for plasmon-enhanced catalysis, interfacial chemical reactions, and hyperthermia.

3. Conclusion

We have established a quantitative nanothermometry method based on DNA-PAINT to probe the interfacial temperature of single nanoparticles in real-time. We demonstrate that the interfacial temperature of single nanoparticles can be tracked on timescales of 3–5 min with a precision of ≈1 K. The precision is largely dictated by slight particle-to-particle differences in τ_{on} that we attribute to differences in DNA density and conformation on individual particles. We further used this method to study the interplay between plasmon-enhanced fluorescence and particle heating, where we find fluorescence intensities up to 10^6 photons s^{-1} K^{-1} in good agreement with simulations. Using dynamic DNA interactions to quantify the local temperature provides a method that is insensitive to the thermal and optical properties of the sample, and is therefore easily extended to other photonic and non-photonic structures alike. For example, the method may be used to quantify the extent to which different substrates affect the interfacial temperature of nanostructures, to probe the temperature of molecular biosensors, to probe the effect of laser pulse length and frequency, or to disentangle contributions from photothermal heating and hot electrons in plasmon-enhanced catalysis.

4. Experimental Section

Sample Preparation for Single-NP Spectroscopy and DNA-PAINT: Borosilicate coverslips (thickness #1.5) were sonicated in methanol for 15 min and dried under nitrogen flow. The coverslips were hydrophylized by plasma treatment for 1 min. The coverslips were thiolated by immersion in a solution of MPTMS (5 vol%) in ethanol for 3 min, after which they were rinsed with ethanol and dried under nitrogen flow.

A suspension of AuNRs (A12-40-700-CTAB, NanoPartz) was centrifuged for 3 min at 10000 rpm and resuspended in 1 mM cetyltrimethylammonium bromide (CTAB) in distilled water. The AuNRs were then spin coated onto the coverslips, after which excess CTAB and unbound nanorods were removed by rinsing with methanol, phosphate buffered saline (PBS), and distilled water.

Sample chambers were prepared from two coverslips (one containing nanorods, the other clean) separated by double-sided tape. The nanorods were functionalized with DNA (IDT Technology) by incubating in 5 μM thiolated docking strands and 1 mM tris(2-carboxyethyl) phosphine hydrochloride in citrate buffer (100 mM, pH 3, 1 M NaCl) for 1–2 h. After incubation, the sample chamber was rinsed with 200 μL of PBS and 200 μL of buffer B (5 mM Tris-HCl, 10 mM MgCl₂, 1 mM EDTA, pH 8.0, filtered). Finally, the chamber was rinsed with 400 μL imager solution (500–600 pM Atto655-conjugated imager strands (Eurofins Genomics) in buffer B), and sealed with tape. All DNA sequences are given in Table S1, Supporting Information.

Single-NP Dark-Field Spectroscopy: Single-NP spectra were measured by objective-type total internal reflection microscopy on an inverted wide-field microscope (Nikon Ti2). The sample was illuminated by a collimated white-light source (Energetiq) through an oil-immersion 1.49 NA objective. The direct reflection was blocked by a beam block after which the scattered light was projected onto an EMCCD camera (Andor iXon Ultra DU-888). Bandpass filters of varying wavelengths were sequentially inserted into the detection path, after which the scattered intensity as a function of wavelength was obtained by fitting a 2D Gaussian to the point spread function.

DNA-PAINT Measurements: DNA-PAINT measurements were performed on the same microscope using a 637 nm excitation laser (OBIS FP 637LX, Coherent). The sample was illuminated using

s-polarized laser light via a dichroic mirror (ZT640rdc, Chroma). The excitation light was further suppressed by a notch filter (ZET635NF, Chroma) and a long-pass filter.

The local excitation power density was determined by fitting the weak background emission from the glass coverslip using a Gaussian function. The position-dependent power density (in W m^{-2}) was calculated as $I = f \frac{P}{2\pi\sigma^2} \exp\left(-\frac{r^2}{2\sigma^2}\right)$, with P the laser power in W, σ the beam radius in the focal plane, r the distance from the beam center, and $f = 3$, a correction factor for an s-polarized evanescent field and a TIRF angle of 65°.[51] Fluorescence data were analyzed using home-made Python and Matlab software (see the Supporting Information for details).

Bulk temperature control was achieved using a home-built temperature-controlled stage with Peltier cooling/heating (see Figures S8 and S9, Supporting Information, for details on the temperature setting).[52]

Numerical Simulations: Simulations of the optical properties of NPs were carried out using the boundary element method (BEM), using the MNPBEM17 toolbox. The nanorod was modeled as a cylinder capped by hemispheres. The dielectric functions of gold and silver were used as tabulated by Johnson & Christy, whereas the refractive index of the medium was set to 1.33; for simplicity the substrate was neglected in the BEM simulations.

The temperature profile near the nanorod was simulated using COMSOL Multiphysics. The nanorod was again modeled as a cylinder capped by hemispheres, with a thermal conductivity of 317 W mK^{-1} (gold) for the NP, 1.14 W mK^{-1} for the borosilicate glass substrate, and 0.59 W mK^{-1} for the aqueous medium. The temperature rise 100 µm away from the rod was set to zero and Poisson's equation was solved numerically. See Figures S4 and S5, Supporting Information, for more details on the simulations.

Statistical Analysis: Uncertainty values on single-particle temperatures were calculated as described in the Supporting Information. The error bars in Figure 2d represent the standard deviation calculated from 32 particles. The value of 0.7 K mentioned in the text resulted from averaging the six error bars in Figure 2d. The fits in Figure 4b were performed in Origin (Levenberg–Marquardt fitting, no weighting) and the standard errors from these fits are shown as the error bars in Figure 4c.

Supporting Information

Supporting Information is available from the Wiley Online Library or from the author.

Acknowledgements

Conflict of Interest

The authors declare no conflict of interest.

Data Availability Statement

Research data are not shared.

[1] H. Altug, S.-h. Oh, S. A. Maier, J. Homola, *Nat. Nanotechnol.* **2022**, *17*, 5.

[2] A. G. Skirtach, A. Muñoz Javier, O. Kreft, K. Köhler, A. Piera Alberola, H. Möhwald, W. J. Parak, G. B. Sukhorukov, *Angew. Chem., Int. Ed.* **2006**, *45*, 4612.

[3] C. M. Pitsillides, E. K. Joe, X. Wei, R. R. Anderson, C. P. Lin, *Biophys. J.* **2003**, *84*, 4023.

[4] L. R. Hirsch, R. J. Stafford, J. A. Bankson, S. R. Sershen, B. Rivera, R. E. Price, J. D. Hazle, N. J. Halas, J. L. West, *Proc. Natl. Acad. Sci. U. S. A.* **2003**, *100*, 13549.

[5] X. Huang, W. Qian, I. H. El-Sayed, M. A. El-Sayed, *Lasers Surg. Med.* **2007**, *39*, 747.

[6] S. Wilhelm, A. J. Tavares, Q. Dai, S. Ohta, J. Audet, H. F. Dvorak, W. C. W. Chan, *Nat. Rev. Mater.* **2016**, *1*, 16014.

[7] J. Morales-Dalmau, C. Vilches, I. De Miguel, V. Sanz, R. Quidant, *Nanoscale* **2018**, *10*, 2632.

[8] P. Zijlstra, M. Orrit, *Rep. Prog. Phys.* **2011**, *74*, 10.

[9] A. Al-Zubeidi, L. A. McCarthy, A. Rafiei-Miandashti, T. S. Heiderscheit, S. Link, *Nanophotonics* **2021**, *10*, 1621.

[10] A. Kinkhabwala, Z. Yu, S. Fan, Y. Avlasevich, K. Müllen, W. E. Moerner, *Nat. Photonics* **2009**, *3*, 654.

[11] D. Punj, M. Mivelle, S. B. Moparthi, T. S. Van Zanten, H. Rigneault, N. F. Van Hulst, M. F. García-Parajó, J. Wenger, *Nat. Nanotechnol.* **2013**, *8*, 512.

[12] L. Su, H. Yuan, G. Lu, S. Rocha, M. Orrit, J. Hofkens, H. Uji-I, *ACS Nano* **2016**, *10*, 2455.

[13] E. Wientjes, J. Renger, R. Cogdell, N. F. Van Hulst, *J. Phys. Chem. Lett.* **2016**, *7*, 1604.

[14] A. F. Koenderink, *ACS Photonics* **2017**, *4*, 710.

[15] Y. Wang, M. Horáček, P. Zijlstra, *J. Phys. Chem. Lett.* **2020**, *11*, 1962.

[16] M. A. Beuwer, M. W. Prins, P. Zijlstra, *Nano Lett.* **2015**, *15*, 3507.

[17] M. Sriram, K. Zong, S. R. Vivekchand, J. Justin Gooding, *Sensors* **2015**, *15*, 25774.

[18] A. B. Taylor, P. Zijlstra, *ACS Sens.* **2017**, *2*, 1103.

[19] G. Baffou, F. Cichos, R. Quidant, *Nat. Mater.* **2020**, *19*, 946.

[20] P. Zijlstra, P. M. Paulo, M. Orrit, *Nat. Nanotechnol.* **2012**, *7*, 379.

[21] J. H. Lee, Z. Cheglakov, J. Yi, T. M. Cronin, K. J. Gibson, B. Tian, Y. Weizmann, *J. Am. Chem. Soc.* **2017**, *139*, 8054.

[22] G. Qiu, Z. Gai, Y. Tao, J. Schmitt, G. A. Kullak-Ublick, J. Wang, *ACS Nano* **2020**, *14*, 5268.

[23] L. Cao, D. N. Barsic, A. R. Guichard, M. L. Brongersma, *Nano Lett.* **2007**, *7*, 3523.

[24] S. H. Askes, E. C. Garnett, *Adv. Mater.* **2021**, *33*, 2105192.

[25] Z. Zhou, E. Sakr, Y. Sun, P. Bermel, *Nanophotonics* **2016**, *5*, 1.

[26] Z. Omair, G. Scranton, L. M. Pazos-Outón, T. P. Xiao, M. A. Steiner, V. Ganapati, P. F. Peterson, J. Holzrichter, H. Atwater, E. Yablonovitch, *Proc. Natl. Acad. Sci. U. S. A.* **2019**, *116*, 15356.

[27] L. Jauffred, A. Samadi, H. Klingberg, P. M. Bendix, L. B. Oddershede, *Chem. Rev.* **2019**, *119*, 8087.

[28] A. Carattino, M. Caldarola, M. Orrit, *Nano Lett.* **2018**, *18*, 874.

[29] S. Jones, D. Andrén, P. Karpinski, M. Käll, *ACS Photonics* **2018**, *5*, 2878.

[30] M. Barella, I. L. Violi, J. Gargiulo, L. P. Martinez, F. Goschin, V. Guglielmotti, D. Pallarola, S. Schlucker, M. Pilo-Pais, G. P. Acuna, S. A. Maier, E. Cortes, F. D. Stefani, *ACS Nano* **2021**, *15*, 2458.

[31] G. Baffou, *ACS Nano* **2021**, *15*, 5785.

[32] G. Baffou, P. Bon, J. Savatier, J. Polleux, M. Zhu, M. Merlin, H. Rigneault, S. Monneret, *ACS Nano* **2012**, *6*, 2452.

[33] A. P. Bell, J. A. Fairfield, E. K. McCarthy, S. Mills, J. J. Boland, G. Baffou, D. McCloskey, *ACS Nano* **2015**, *9*, 5551.

[34] L. Priest, J. S. Peters, P. Kukura, *Chem. Rev.* **2021**, *121*, 11937.

[35] J. Zhou, B. del Rosal, D. Jaque, S. Uchiyama, D. Jin, *Nat. Methods* **2020**, *17*, 967.

[36] L. M. Maestro, P. Haro-González, J. G. Coello, D. Jaque, *Appl. Phys. Lett.* **2012**, *100*, 20.

[37] M. J. Chiu, L. K. Chu, *Phys. Chem. Chem. Phys.* **2015**, *17*, 17090.

[38] Q. Jiang, B. Rogez, J. B. Claude, G. Baffou, J. Wenger, *ACS Photonics* **2019**, *6*, 1763.

[39] G. Baffou, M. P. Kreuzer, F. Kulzer, R. Quidant, *Opt. Express* **2009**, *17*, 3291.

[40] S. Ebrahimi, Y. Akhlaghi, M. Kompany-Zareh, Å. Rinnan, *ACS Nano* **2014**, *8*, 10372.

[41] G. Wang, Z. Li, X. Luo, R. Yue, Y. Shen, N. Ma, *Nanoscale* **2018**, *10*, 16508.

[42] D. A. Hastman, J. S. Melinger, G. L. Aragonés, P. D. Cunningham, M. Chiriboga, Z. J. Salvato, T. M. Salvato, C. W. Brown, D. Mathur, I. L. Medintz, E. Oh, S. A. Diáz, *ACS Nano* **2020**, *14*, 8570.

[43] P. A. Reinhardt, A. P. Crawford, C. A. West, G. DeLong, S. Link, D. J. Masiello, K. A. Willets, *J. Phys. Chem. B* **2021**, *125*, 12197.

[44] R. Jungmann, C. Steinhauer, M. Scheible, A. Kuzyk, P. Tinnefeld, F. C. Simmel, *Nano Lett.* **2010**, *10*, 4756.

[45] L. E. Morrison, L. M. Stols, *Biochemistry* **1993**, *32*, 3095.

[46] P. J. Sanstead, A. Tokmakoff, *J. Phys. Chem. B* **2018**, *122*, 3088.

[47] M. Horáček, D. J. Engels, P. Zijlstra, *Nanoscale* **2020**, *12*, 4128.

[48] X. Lu, G. Ye, D. Punj, R. C. Chiechi, M. Orrit, *ACS Photonics* **2020**, *7*, 2498.

[49] A. Puchkova, C. Vietz, E. Pibiri, B. Wünsch, M. Sanz Paz, G. P. Acuna, P. Tinnefeld, *Nano Lett.* **2015**, *15*, 8354.

[50] F. Schueder, J. Stein, F. Stehr, A. Auer, B. Sperl, M. T. Strauss, P. Schwille, R. Jungmann, *Nat. Methods* **2019**, *16*, 1101.

[51] M. Martin-Fernandez, C. Tynan, S. Webb, *J. Microsc.* **2013**, *252*, 16.

[52] R. P. Tas, M. M. R. M. Hendrix, I. K. Voets, bioRxiv:10.1101/2022.04.05.487137, **2022**.